Grain shape effects in bed load sediment transport (pre-print)

Eric Deal[1]*, Jeremy G. Venditti[2,3], Santiago J. Benavides[1], Ryan Bradley[2,3,4], Qiong Zhang[5], Ken Kamrin[5], J. Taylor Perron[1]

[1]Department of Earth, Atmospheric and Planetary Sciences, Massachusetts Institute of Technology, Cambridge, MA, USA
[2]Department of Geography, Simon Fraser University, Burnaby, BC, Canada
[3]School of Environmental Science, Simon Fraser University, Burnaby, BC, Canada
[4]Northwest Hydraulic Consultants, North Vancouver, BC, Canada
[5]Department of Mechanical Engineering, Massachusetts Institute of Technology, Cambridge, MA, USA

*Corresponding author: eric.deal@erdw.ethz.ch

Grain shape effects in bed load sediment transport

Eric Deal[1]*, Jeremy G. Venditti[2,3], Santiago J. Benavides[1], Ryan Bradley[2,3,4], Qiong Zhang[5], Ken Kamrin[5], J. Taylor Perron[1]

[1]Department of Earth, Atmospheric and Planetary Sciences, Massachusetts Institute of Technology, Cambridge, MA, USA
[2]Department of Geography, Simon Fraser University, Burnaby, BC, Canada
[3]School of Environmental Science, Simon Fraser University, Burnaby, BC, Canada
[4]Northwest Hydraulic Consultants, North Vancouver, BC, Canada
[5]Department of Mechanical Engineering, Massachusetts Institute of Technology, Cambridge, MA, USA

Bed load sediment transport, in which wind or water flowing over a bed of sediment causes grains to roll or hop along the bed, is a critically important mechanism in contexts ranging from river restoration[1] to planetary exploration[2]. Despite its widespread occurrence, predictions of bed load sediment flux are notoriously imprecise[3,4]. Many studies have focused on grain size variability[5-7] as a source of uncertainty, but few have investigated the role of grain shape, even though shape has long been suspected to influence transport rates[8]. Here we show that grain shape can modify bed load transport rates by an amount comparable to the scatter in many sediment transport data sets[4,9,10]. We develop a theory that accounts for grain shape effects on fluid drag and granular friction and predicts that the onset and efficiency of bed load transport depend on the mean drag coefficient and bulk friction coefficient of the transported grains. Laboratory flume experiments using a variety of grain shapes confirm these predictions. We propose a shape-independent sediment transport law that collapses our experimental measurements onto a single trend, allowing for more accurate predictions of sediment transport and helping reconcile theory developed for spherical particle transport with the behavior of natural sediment grains.

Many planetary surfaces are fluid-regolith interfaces where flowing gasses or liquids are in contact with granular sediment. On Earth, the resulting sediment transport down hillslopes, through rivers, along coasts, and across deserts moves vast quantities of rock and other particulate material long distances[3]. Evidence of sediment transport on worlds such as Mars and Titan is used to infer past[11] and present[2] climates and to guide the search for habitable environments[12,13]. In bed load sediment transport, grains roll, hop, and slide while generally remaining in contact with the sediment bed rather than being suspended in the fluid. This mechanism is responsible for moving a landscape's coarsest grains, and it plays an outsized role in shaping mountainous regions and building Earth's sedimentary record[14]. Bed load transport also plays a critical role in numerous environmental and engineering contexts, including river delta formation[15], natural hazard mitigation[16] and recovery, pollutant transport[17], infrastructure projects[18], and restoration of rivers and coasts[1].

Despite nearly a century of research on bed load transport[6,8,9,19,20], sediment flux predictions can be highly uncertain, with typical errors up to a factor of five or more[4,10]. It has proven difficult to develop simple yet accurate models of bed load transport, which involves fully turbulent fluid flow interacting with a dense sediment slurry[3]. Widely used models are semi-empirical and typically predict sediment flux based on average flow and bed conditions as

$$q^* = \alpha(\tau^* - \tau_c^*)^{\frac{3}{2}} \quad (1)$$

where q^* is the nondimensional volumetric sediment flux per unit width of river bed, τ^*, the Shields number, is the nondimensional shear stress on the bed (Methods), τ_c^* is the critical Shields

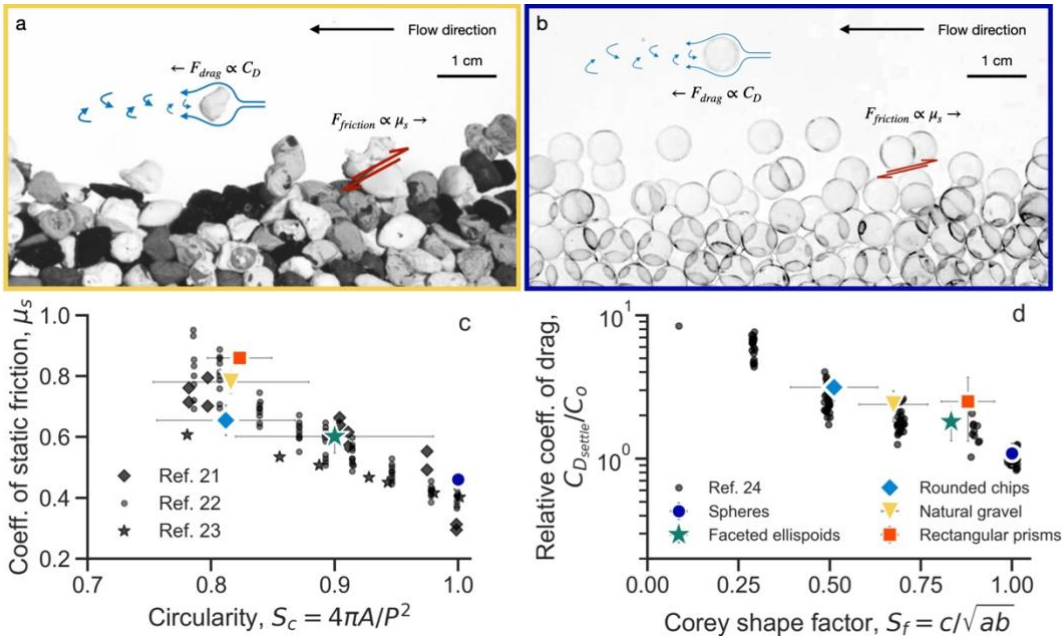

Fig. 1 | Competing effects of grain shape on bed load sediment transport. a, Image of natural gravel undergoing bed load transport highlighting the forces due to fluid drag and grain-grain friction. **b,** Same as **a**, but with spheres. **c**, Comparison of bulk coefficient of static friction with a measure of grain shape - circularity, $S_C = 4\pi A/P^2$, where *A* is the projected grain area and *P* is the projected perimeter (values closer to 1 indicate more spherical grains), for a compilation of observations[21-23] and the materials used in our experiments. **d**, Comparison of the still-water-settling drag coefficient, $C_{D_{\text{settle}}}$, normalized by the drag coefficient for a sphere of the same volume (Methods) with a measure of grain shape - the Corey shape factor, $S_f = c/\sqrt{ab}$, where *a*, *b*, and *c* are the long, intermediate, and short axes of a grain, for a compilation of observations[24] and the materials used in our experiments.

number below which no transport occurs, and α is a constant that describes sediment transport efficiency.

The variability in grain size, shape and density found in nature makes it difficult to use models like equation (1) to predict sediment transport accurately across a wide range of settings[4,25]. Size[5-7] and density[8,26] effects on grain motion are well studied, and both appear in the standard nondimensionalization of the problem (equation (1); Methods). Still, grain size effects have drawn continued attention as a remaining source of uncertainty[3,5,6]. In contrast, the effects of grain shape have received little attention until recently[27,28], despite the fact that shape has long been hypothesized to influence transport rates and dynamics[8]. Recent theoretical work on bed load transport supplements the traditional continuum mechanics approach with techniques from granular physics[29,30], but these approaches generally assume that grains are spherical. Empirical sediment transport models, on the other hand, are generally calibrated with and applied to aspherical natural materials. Understanding grain shape effects will bridge the gap between theoretical studies of idealized grains and real-world applications.

During bed load transport, the granular bed is sheared by the flow passing over it. Aspherical grains and rough surfaces generally increase the resistance to such shearing[31], and the tendency of aspherical grains to slide along the bed rather than roll further enhances frictional resistance. This argument is consistent with a compilation of bulk friction coefficients showing that less spherical granular materials generally have higher friction

coefficients (Fig. 1c). The idea that aspherical grains are harder to transport is also in line with recent work which finds that individual aspherical grains are transported more slowly than their spherical counterparts[27].

However, aspherical grains experience higher fluid drag force than spherical grains of the same volume[24,32-34], resulting in more efficient fluid-grain momentum transfer under the same flow conditions. This occurs not only because irregular grain shapes generally impede flow around the grain, but also because grains in the flow tend to reorient such that their largest cross-sectional area is perpendicular to the flow[35]. This argument is consistent with the observation that spherical grains settle faster in still water than other natural, convex shapes, i.e. more aspherical grains generally exhibiting slower settling velocities (Fig. 1d). Enhanced fluid drag on aspherical grains counteracts the enhanced granular friction, partially obscuring the relation between grain shape and bed load transport parameters. These competing effects of grain shape make it challenging to understand the net effect of grain shape on sediment transport.

A shape-independent sediment transport law

We disentangle these competing effects by formulating a theory that accounts for grain shape effects on both fluid-grain and grain-grain interactions. We assume that the fluid drag forces driving grain motion can be described with an effective coefficient of drag (C_D) and that the resistance to bed load motion due to granular contacts can be described with a bulk friction coefficient (μ_s). The derivation of the Shields number reveals how drag and friction coefficients should influence the transport coefficient α and entrainment threshold τ_c^* in equation (1). In the standard derivation the coefficients of drag and friction are dropped, yet these are precisely the parameters sensitive to grain shape. We retain these terms to modify the conventional Shields number, multiplying it by a ratio of two dimensionless quantities that account for drag and friction.

The first quantity, C^*, is the effective drag coefficient normalized by the drag coefficient of the volume-equivalent sphere (denoted with the subscript o): $C^* = C_D/C_o = S_f C_{D_{\text{settle}}}/C_o$. The effective drag coefficient C_D is obtained by multiplying the drag coefficient of grains settling in still water, $C_{D_{\text{settle}}}$, by the Corey shape factor, S_f, to account for the fact that grains tumble during transport (Methods). The second quantity, μ^*, is the average bulk friction coefficient normalized by the bulk friction coefficient of spheres, both modified by the tangent of the bed angle θ to account for a tilted bed: $\mu^* = (\mu_s - \tan\theta)/(\mu_o - \tan\theta)$. Both C^* and μ^* are equal to one for spheres and increase as grains become more aspherical.

Introducing the shape-independent Shields number $(C^*/\mu^*)\tau^*$ (Methods) yields a shape-independent bed load transport law,

$$q^* = \alpha_o \left(\frac{C^*}{\mu^*}\tau^* - \tau_{co}^*\right)^{\frac{3}{2}} \quad (2)$$

where the parameters α_o and τ_{co}^* are the transport coefficient and threshold of motion for spheres. Comparing equation (2) with the standard bed load transport law (equation (1)) shows how the conventional transport coefficient and threshold of motion depend on grain shape: $\alpha = \alpha_o(C^*/\mu^*)^{3/2}$ and $\tau_c^* = \tau_{co}^*(\mu^*/C^*)$. Equation (2) predicts that the sediment flux q^* for a given shape-independent Shields number should be the same regardless of grain shape.

This approach also makes it possible to observe separately the competing effects of grain shape on bulk friction and fluid drag. Anticipating that the enhanced bulk friction of more aspherical grains outweighs the enhanced fluid drag[27] we rewrite equation (1) in terms of a modified boundary shear stress $C^*\tau^*$, which corrects for the effect of grain shape on fluid drag forces only:

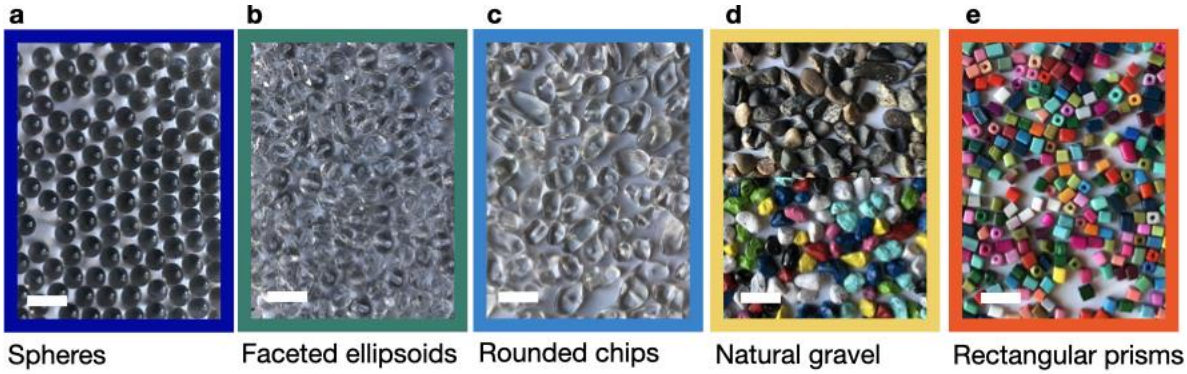

Fig. 2 | Granular materials used in the experiments. a, Spheres. **b,** Faceted ellipsoids. **c**, Rounded chips. **d**, Unpainted (top) and painted (bottom) natural gravel. Painted gravel was used in the experiments to aid automated grain identification. **e**, Rectangular prisms. White scale bars are 1 cm. Materials in a and b have uniform grain shapes, whereas shapes of the materials in c, d, and e vary from grain to grain.

$$q^* = \frac{\alpha}{C^{*3/2}}(C^*\tau^* - C^*\tau_c^*)^{\frac{3}{2}}. \quad (3)$$

Equation (3) predicts that variations in sediment flux q^* for a given value of $C^*\tau^*$ should only reflect differences in bulk grain friction. Accordingly, the modified transport coefficient and threshold of motion in equation (3) are expected to be functions of μ^* only. Using the relationships for α and τ_c^* above, we obtain $C^*\tau_c^* = \tau_{co}^*\mu^*$ and $\alpha/C^{*3/2} = \alpha_o/\mu^{*3/2}$. Given measurements of bed load sediment flux over a range of bed shear stress for granular materials with different shapes, we can test these predictions and estimate the values of α_o and τ_{co}^* by fitting equation (3) to plots of q^* against $C^*\tau^*$. Knowing α_o and τ_{co}^*, we can then test whether the shape-independent transport law (equation (2)) successfully predicts sediment flux for all grain shapes.

Laboratory flume experiments

We conducted a series of flume experiments with five granular materials of similar size and density but different shapes (Fig. 2; Methods). In each experiment, we supplied a constant water discharge and sediment feed at the upstream end of a narrow (2-3 grain diameters wide), inclined flume and made measurements after the system had reached an equilibrium in which sediment outflux matched sediment influx. All five granular materials exhibit the scaling between dimensionless sediment flux and Shields number predicted by equation (1) (Fig. 3a). However, the dimensionless sediment flux for spheres is higher than for natural gravel by a factor of at least 2.5 for the same Shields number, with an even larger difference close to the threshold of motion, demonstrating that grain shape has an important influence on bed load transport.

Plotting sediment flux as a function of the drag-corrected Shields number, $C^*\tau^*$, reveals the full effect of shape-dependent bulk friction on bed load transport. More aspherical granular materials are substantially more resistant to transport for a given $C^*\tau^*$ (Fig. 3b). By fitting equation (3) to the data in Fig. 3b, we extract the drag-corrected coefficient of transport, $\alpha/C^{*3/2}$, and the drag-corrected threshold of motion, $C^*\tau_c^*$, for each granular material.

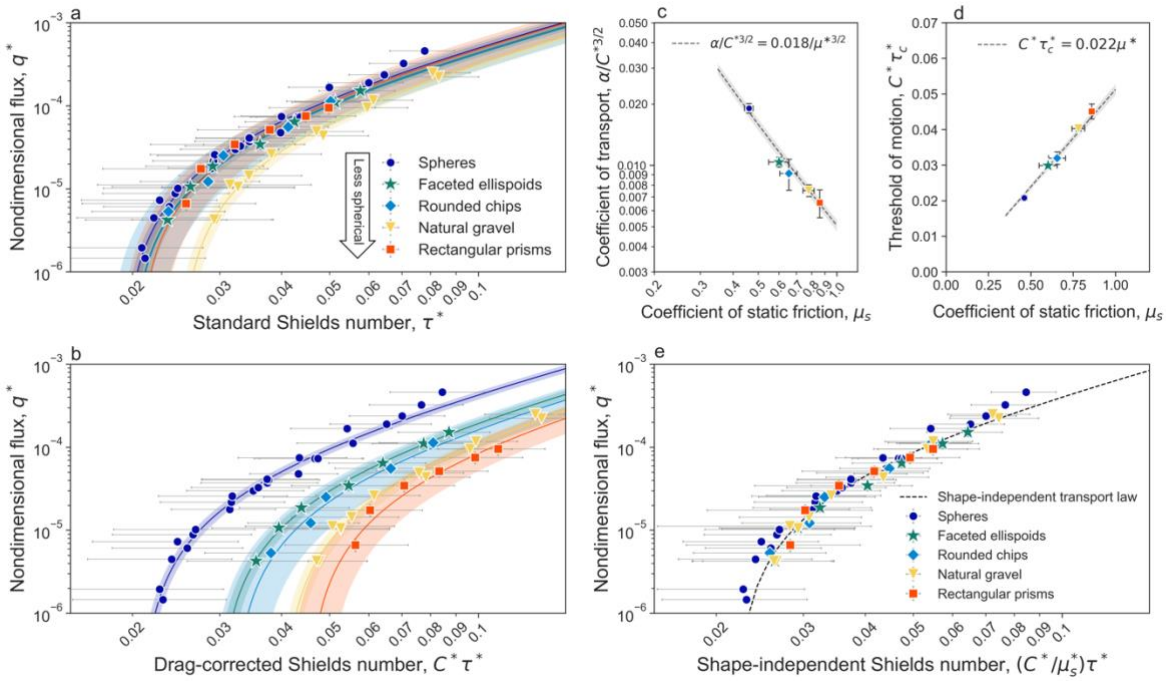

Fig. 3 | Comparison of grain shape theory with laboratory flume data. a, Nondimensional sediment flux (q^*) as a function of the conventional Shields number (τ^*) for the five granular materials in Fig. 2. Lines are fits of equation (1). **b**, Nondimensional sediment flux as a function of drag-corrected Shields number, $C^*\tau^*$. **c**, Drag-corrected sediment transport coefficient as a function of bulk friction coefficient. **d**, Drag-corrected threshold of sediment motion (see equation 3) as a function of bulk friction coefficient. Values of $\alpha/C^{*3/2}$ and $w^*\tau_c^*$ plotted in **c** and **d** are from the fits in **b**. **e**, Nondimensional sediment flux as a function of shape-independent Shields number, $(C^*/\mu^*)\tau^*$. Dashed line is equation (2) with α_o and τ_{co}^* determined from the fits in **c** and **d.** Error bars show one standard error of the mean. Shaded regions are 95% confidence intervals.

Both drag-corrected quantities scale as predicted with μ^*, and therefore also with $\mu_s - \tan\theta$, since $\mu^* \propto \mu_s - \tan\theta$ (Fig. 3c,d; Methods). Specifically, the modified transport coefficient $\alpha/C^{*3/2}$ scales with $\mu^{*-3/2}$ (Fig. 3c), implying that frictionally stronger granular materials have lower bed load transport rates. The modified threshold of motion $C^*\tau_c^*$ scales linearly with μ^* (Fig. 3d), implying that frictionally stronger granular materials require proportionally higher shear stress to initiate sediment transport. This observation is consistent with previous predictions for the threshold of motion[36-38] as well as the prediction from our grain shape theory, which can be simplified to (Methods)

$$\tau_c^* = (\mu^*/C^*)\tau_{co}^* \propto \frac{\mu_s - \tan\theta}{c_D}. \quad (4)$$

With this parameterization of fluid drag and grain friction as a function of grain shape, we compare the shape-independent transport law (equation (2)) with the flume experiments. Plotting nondimensional sediment flux as a function of the shape-independent Shields number $(C^*/\mu^*)\tau^*$, which accounts for the effects of grain shape on both fluid drag and granular friction, confirms that the five granular materials in our experiments collapse to a

single trend with error similar to that of each grain type on its own (standard error of Fig. 3e: 1.6×10^{-6}, mean of standard errors of the five fits in Fig. 3a: 2.2×10^{-6}). The match between the shape-independent theory and experimental data, along with the observation that a single coefficient and entrainment threshold collapse all five granular materials, indicate that our theoretical approach successfully accounts for the net effects of grain shape on bed load transport for sediment grains with a wide range of shapes. It is informative to compare this result with efforts to account for grain shape effects on the entrainment threshold alone, which can partially explain differing transport rates of differently shaped grains[27]. The single trend in Fig. 3a shows that fluid and frictional effects during both entrainment and subsequent transport must be accounted for to fully reconcile transport rates of different grain shapes.

Implications for sediment transport models and predictions

Our experiments demonstrate that grain shape has a substantial effect on bed load sediment entrainment and transport. Sediment flux varies by a factor of at least 2.5 for the same Shields number across the five grain shapes (Fig. 3a), consistent with the observation that isolated spherical grains move downstream faster than aspherical grains in the same flow[27]. Close to the threshold of entrainment ($\tau^* \lesssim 0.03$ in our experiments), a condition typical of bed load transport in gravel-bed rivers[39], the range increases to a factor of five or more. This magnitude of variability in transport rate for the same Shields number is comparable to that observed in compilations of flume data[4,9,10], suggesting that grain shape effects may underlie some of this scatter.

The magnitude of the grain shape effect in our experiments does not necessarily translate directly to natural scenarios, because the five granular materials do not mimic the greater range of natural grain shapes. Although the abrasion that occurs during sediment transport can lead to convergence in shape[41-43], natural sediment grains take on a variety of shapes due to the varied mechanical properties of their source rocks and transport conditions[40]. Still, some of the most common naturally occurring shapes are present in our experimental materials. These include platy grains derived from bedded or foliated rocks (rounded chips), grains with faceted mineral surfaces (faceted ellipsoids), blocky grains formed by intersecting fracture planes (rectangular prisms), well-rounded grains (spheres), and partially rounded grains (natural gravel).

The largest difference in transport rate observed in our experiments is between spheres and natural river gravel (Fig. 3a, b), which may be representative, or even an underestimate, of the range of grain rounding found in nature. Comparison of Figs. 3a and 3b suggests that enhanced fluid drag due to aspherical grains is not as effective at offsetting enhanced granular friction in natural gravel as it is in the other aspherical materials in our experiments. We suspect that the reduced influence of drag is due to the surface properties of the natural gravel, which could be the product of a feedback in which abrasion[42] during sediment transport drives grains towards lower-drag shapes that are less likely to be entrained subsequently. The difference between spheres and natural gravel is also important because spheres are a favored tool in theoretical and experimental studies of sediment transport. Our results imply that inferences based on spheres may not translate directly to natural sediment, but our theory provides a framework for making such comparisons.

In summary, we find that differences in the efficiency of bed load transport and the threshold of motion among different grain shapes can be reconciled by modifying the Shields number to account for enhanced fluid drag (via C^*) and bulk friction (via μ^*) in more aspherical grains. These competing effects of grain shape can be characterized with familiar, easily measured quantities: the coefficients of drag and bulk friction. Although this approach does not capture all the possible effects of grain shape[44], the ability to account for grain shape in sediment transport calculations is a major improvement over the usual practice of

ignoring it. Better predictions of bed load flux (Fig. 3e) will aid interpretations of the sedimentary record and studies of landscape evolution, as well as benefiting environmental applications such as river restoration[1], coastal engineering[45,46], and contaminant transport[17]. A better understanding of the bulk transport dynamics of aspherical grains also has broader applications ranging from prediction of volcanic hazards[47] to industrial and agricultural processes[48] involving granular materials. Our approach is simple enough to apply to grain shapes observed elsewhere in the solar system[49-50] and could help improve reconstructions of past and present climate on worlds such as Mars and Titan.

References

1. Simon, A., Bennett, S. J. & Castro, J. M. *Stream Restoration in Dynamic Fluvial Systems*. (2013). doi:10.1029/gm194.
2. Perron, J. T. *et al.* Valley formation and methane precipitation rates on Titan. *J Geophys Res Planets 1991 2012* 111, (2006).
3. Garcia, M. H. (2008). Sedimentation Engineering Processes, Measurements, Modelling and Practice, 1050 pp., Am. Soc. Civ. Eng., Reston, Va..
4. Gomez, B. & Church, M. An assessment of bedload sediment transport formulae for gravel bed rivers. *Water Resour Res* 25, 1161–1186 (1989).
5. Wilcock, P. R. & Crowe, J. C. Surface-based Transport Model for Mixed-Size Sediment. *J Hydraul Eng* 129, 120–128 (2003).
6. Parker, G., Klingeman, P. C. & McLean, D. G. Bedload and Size Distribution in Paved Gravel-Bed Streams. *J Hydraulics Div* 108, 544–571 (1982).
7. Proffitt, G. T. & Sutherland, A. J. TRANSPORT OF NON-UNIFORM SEDIMENTS. *J Hydraul Res* 21, 33–43 (1983).
8. Shields, A. Application of similarity principles and turbulence research to bedload movement. (1936).
9. Wong, M. & Parker, G. Reanalysis and Correction of Bed-Load Relation of Meyer-Peter and Müller Using Their Own Database. *J Hydraul Eng* 132, 1159–1168 (2006).
10. Frey, P., and Church, M. "How river beds move." *Science* 325.5947 (2009): 1509-1510.
11. Dietrich, W. E., et al. "Fluvial gravels on Mars: Analysis and implications." *Gravel-Bed Rivers: Processes and Disasters* (2017): 755-783.
12. Grotzinger, J. P., et al. "A habitable fluvio-lacustrine environment at Yellowknife Bay, Gale Crater, Mars." *Science* 343.6169 (2014).
13. Goudge, T.A., et al. "Stratigraphy and paleohydrology of delta channel deposits, Jezero crater, Mars." *Icarus* 301 (2018): 58-75.
14. Church, M. "Bed material transport and the morphology of alluvial river channels." *Annu. Rev. Earth Planet. Sci.* 34, (2006): 325–-354 (2006)..
15. Nienhuis, J. H. *et al.* Global-scale human impact on delta morphology has led to net land area gain. *Nature* 577, 514–518 (2020).
16. Alcántara-Ayala, I. Geomorphological Hazards and Disaster Prevention. 269–278 (2009) doi:10.1017/cbo9780511807527.022.
17. Whyte, D. C. & Kirchner, J. W. Assessing water quality impacts and cleanup effectiveness in streams dominated by episodic mercury discharges. *Sci Total Environ* 260, 1–9 (2000).
18. Gilvear, D. J. Fluvial geomorphology and river engineering: future roles utilizing a fluvial hydrosystems framework. *Geomorphology* 31, 229–245 (1999).
19. E., Meyer-Peter. & R., Müller. Formulas for Bed-Load transport. *Hydraulic Engineering Reports* (1948).
20. Bagnold, R. A. *An approach to the sediment transport problem from general physics*. US government printing office, 1966.
21. Carrigy, M. A. Experiments on the Angles of Repose of Granular Materials. *Sedimentology* **14**, 147–158 (1970).
22. Dai, B. B., Yang, J. & Zhou, C.-Y. Micromechanical origin of angle of repose in granular materials. *Granul Matter* **19**, 24 (2017).
23. Mead, S. R., Cleary, P. W. & Robinson, G. K. Characterising the failure and repose angles of irregularly shaped three-dimensional particles using DEM. (2012).
24. Dietrich, W. E. Settling velocity of natural particles. *Water Resour Res* 18, 1615–1626 (1982).
25. Reid, I, and Jonathan B. L. "Bed load sediment transport in an ephemeral stream and a comparison with seasonal and perennial counterparts." *Water Resources Research* 31.3 (1995): 773-781.
26. Low, H. S. Effect of Sediment Density on BedLoad Transport. *J Hydraul Eng* 115, 124–138 (1989).
27. Cassel, M., et al. Bedload transport in rivers, size matters but so does shape. *Sci Rep-uk* 11, 508 (2021).
28. Dudill, A., et al. "Comparing the behaviour of spherical beads and natural grains in bedload mixtures." *Earth Surface Processes and Landforms* 45.4 (2020): 831-840.
29. Furbish, D., et al. A probabilistic description of the bedload sediment flux: 1. Theory. *Journal of Geophysical Research: Earth Surface (2003–2012)* 117, n/a-n/a (2012).
30. Maurin, R., Chauchat, J., & Frey, P. "Revisiting slope influence in turbulent bedload transport: consequences for vertical flow structure and transport rate scaling." *Journal of Fluid Mechanics* 839 (2018): 135-156.
31. Burkalow, A. V. Angle of Repose and Angle of Sliding Friction: An Experimental Study. *Gsa Bulletin* 56, 669–707 (1945).
32. Smith, D. A. & Cheung, K. F. Settling Characteristics of Calcareous Sand. *J Hydraul Eng* 129, 479–483 (2003).
33. Dioguardi, F. & Mele, D. A new shape dependent drag correlation formula for non-spherical rough particles. Experiments and results. *Powder Technol* 277, 222–230 (2015).
34. Göğüş, M., İpekçi, O. N. & Kökpina, M. A. Effect of Particle Shape on Fall Velocity of Angular Particles. *J Hydraul Eng* 127, 860–869 (2001).
35. Middleton, G. V. & Southard, J. B. Mechanics of Sediment Movement. 8-1-8–34 (1984) doi:10.2110/scn.84.03.0008.
36. Egiazaroff, I. V. Calculation of Nonuniform Sediment Concentrations. *J Hydraulics Div* 91, 225–247 (1965).
37. Lamb, M. P., Dietrich, W. E. & Venditti, J. G. Is the critical Shields stress for incipient sediment motion dependent on channel-bed slope? *J Geophys Res Earth Surf 2003 2012* 113, (2008).
38. Wiberg, P. L. & Smith, J. D. Calculations of the critical shear stress for motion of uniform and heterogeneous sediments. *Water Resour Res* 23, 1471–1480 (1987).
39. Parker, G. Self-formed straight rivers with equilibrium banks and mobile bed. Part 2. The gravel river. *J Fluid Mech* 89, 127–146 (1978).
40. Bodek, S., and Jerolmack, D. "Breaking down chipping and fragmentation in sediment transport: the control of material strength." *Earth Surface Dynamics Discussions*(2021): 1-21.
41. Parker, G. Sedimentation Engineering. 165–251 (2008) doi:10.1061/9780784408148.ch03.
42. Domokos, G., et al. "How river rocks round: resolving the shape-size paradox." *PloS one* 9.2 (2014): e88657.
43. Novák-Szabó, T., et al. "Universal characteristics of particle shape evolution by bed-load chipping." *Science advances* 4.3 (2018): eaao4946.

44. Cleary, P. W. The effect of particle shape on simple shear flows. *Powder Technol* 179, 144–163 (2008).
45. Riazi, A., et al. "Improved drag coefficient and settling velocity for carbonate sands." *Scientific reports* 10.1 (2020): 1-9.
46. Soulsby, R. L., and Damgaard, J. S. "Bedload sediment transport in coastal waters." *Coastal Engineering*52.8 (2005): 673-689.
47. Dufek, J., Manga, M. & Patel, A. Granular disruption during explosive volcanic eruptions. *Nat Geosci* 5, 561–564 (2012).
48. Katterfeld, A., and Wensrich, C. "Understanding granular media: from fundamentals and simulations to industrial application." *Granular Matter* 19.4 (2017): 1-4.
49. Tomasko, M. G., et al. "Rain, winds and haze during the Huygens probe's descent to Titan's surface." *Nature* 438.7069 (2005): 765-778.
50. Williams, R., et al. "Martian fluvial conglomerates at Gale crater." *science* 340.6136 (2013): 1068-1072.

Methods

Grain shape theory for bed load transport

Shape-independent Shields number. We derive a shape-independent Shields number by retaining terms describing fluid drag and bulk grain friction in the derivation used to obtain the conventional Shields number. The Shields number compares the magnitudes of forces driving and resisting grain motion. As illustrated in the free-body diagram in Extended Data Figure 1, a spherical grain with diameter d_o and density ρ_s resting on a bed inclined at an angle θ from the horizontal and immersed in a moving fluid with density ρ experiences a gravitational force F_g, a buoyant force F_b, a fluid drag force F_D, a lift force F_L, a bed contact force F_c, and a frictional force F_f. At the threshold of grain motion, the slope-parallel driving and resisting forces are equal in magnitude,

$$\begin{aligned} F_D + \left(F_g - F_b\right)\sin\theta = \mathrm{F_f} \\ = \mu_s\left(\left(F_g - F_b\right)\cos\theta - F_L\right) \end{aligned} \tag{5}$$

where μ is the coefficient of bulk static friction. The force magnitudes are

$$F_D = \frac{1}{2}\rho C_D u^{*2} A \tag{6a}$$
$$F_L = \frac{1}{2}\rho C_L u^{*2} A \tag{6b}$$
$$F_g = \rho_s g V \tag{6c}$$
$$F_b = \rho g V \tag{6d}$$

where C_D is the drag coefficient, C_L is the lift coefficient, V is grain volume, A is grain cross-sectional area, g is gravitational acceleration, and $u^* = \sqrt{\tau/\rho}$, with τ the shear stress due to the flow. For a spherical grain, $A = \pi d_\circ^2/4$ and $V = \pi d_\circ^3/6$. Substituting equations (6a – 6d) into equation (5) and rearranging to obtain a ratio of terms involving drag and lift to terms involving gravity and friction yields a definition of a "complete" Shields number at the threshold of motion,

$$\tau^*_{\mathrm{complete}} = 1 = \frac{3}{4}\frac{(C_D + \mu_s C_L)\tau}{(\rho_s - \rho) g d_\circ \cos\theta\,(\mu_s - \tan\theta)} \tag{7}$$

Equation (7) can alternatively be derived by defining $\tau^*_{\mathrm{complete}}$ as the ratio of driving to resisting forces and assuming flow conditions close to the threshold of motion ($\tau^*_{\mathrm{complete}} \approx 1$). We find that this is also a good approximation for $\tau^*_{\mathrm{complete}} > 1$.

Making the common assumption that the lift term is negligible ($\mu_s C_L \ll C_D$) simplifies this definition to

$$\tau^*_{\mathrm{complete}} \propto \frac{1}{\cos\theta}\frac{C_D}{\mu_s - \tan\theta}\frac{\tau}{(\rho_s - \rho) g d_\circ} \tag{8}$$

Ignoring the terms involving the drag coefficient, the bulk friction coefficient, and the bed slope yields the conventional definition of the Shields number,

$$\tau^*_{\mathrm{conventional}} = \frac{\tau}{(\rho_s - \rho) g d_\circ} \tag{9}$$

We account for grain shape effects by instead retaining the terms involving C_D, μ_s, and θ in equation (8). We additionally multiply by the normalizing factor $\cos\theta\,(\mu_\circ - \tan\theta)/C_\circ$, where μ_o is the coefficient of static friction for spheres and C_o is the drag coefficient of spheres, yielding the shape-independent Shields number:

$$\tau^*_{\text{shape}} = \frac{C_D}{C_o}\frac{\mu_o - \tan\theta}{\mu_s - \tan\theta}\frac{\tau}{(\rho_s - \rho)gd_o} = \frac{C^*}{\mu^*}\tau^*_{\text{conventional}} \quad (10)$$

where the dimensionless quantities C^* and μ^* representing shape-dependent fluid drag and bulk friction are as defined in the main text. The normalizing factor, and the resulting definitions of C^* and μ^*, have the effect that the shape-independent sediment transport model, equation (2), reduces to the conventional model, equation (1), for spheres. In addition, normalizing by C_o ensures that C^* is not a function of grain size, whereas C_D is a function of the particle Reynolds number[41], and therefore implicitly a function of grain size for a given flow. We assume that $C_D = S_f C_{D_{settle}}$. In our experiments with 5 mm spheres, $\mu_o = \tan(24.7°)$ and $C_o = 0.4$ (ref. 24). Interestingly, the dependence on bulk friction in equation (10) is consistent with a two-phase continuum model of sediment transport, which shows that the nondimensional sediment flux, q^*, scales with $\tau^*_{\text{conventional}}/\left(\mu_s(1 - \gamma\tan\theta)\right)$, where $\gamma \approx 2$ (ref. 30).

To incorporate the shape-independent Shields number into a sediment transport model, we multiply the Shields number in equation (1) by $(C^*/\mu^*)\cdot(\mu^*/C^*) = 1$. Moving the (μ^*/C^*) term into the coefficient of transport gives

$$q^* = \frac{\alpha\mu^{*3/2}}{C^{*3/2}}\left(\frac{C^*}{\mu^*}\tau^* - \frac{C^*}{\mu^*}\tau^*_c\right)^{3/2} \quad (11)$$

where the nondimensional volumetric sediment flux per unit width is defined as $q^* = q_s/\sqrt{Rgd_o^3}$, q_s is the dimensional volumetric sediment flux per unit width, $R = (\rho_s - \rho)/\rho$, and the first term in parentheses is the shape-independent Shields number (equation 10). Defining $\alpha_o = \alpha(\mu^*/C^*)^{3/2}$ and $\tau^*_{co} = \tau^*_c(C^*/\mu^*)$ leads to the shape-independent transport law in equation (2).

The shape-independent transport law reveals how the conventional critical Shields number, τ^*_c, depends on the bulk friction coefficient, μ_s. Using the definitions of μ^* and C^*, the expression $\tau^*_c = (\mu^*/C^*)\tau^*_{co}$ can be written as

$$\tau^*_c = \frac{C_o}{C_D}\frac{\mu_s - \tan\theta}{\mu_o - \tan\theta}\tau^*_{co} \quad (12)$$

This can be rearranged to give

$$\tau^*_c = \frac{C_o\tau^*_{co}}{\mu_o - \tan\theta}\frac{\mu_s - \tan\theta}{C_D} \propto \frac{\mu_s - \tan\theta}{C_D} \quad (13)$$

The proportionality holds because the first term is a constant for the same mean bed angle.

Modified drag coefficient. We measured grain drag coefficients, $C_{D_{\text{settle}}}$, by observing the grains settling in still water. Grains tend to settle in still water with their largest projected area perpendicular to the flow[24,35], which is the orientation with the largest drag force. Such a settling orientation is different from grain orientation during bed load transport, where grains tumble, presenting all faces to the flow. The measured drag coefficient for grain settling is therefore relevant to, but larger than, the effective drag coefficient during bed load transport.

To correct our measured drag coefficients for the effect of settling orientation while retaining the influence of other aspects of grain shape, we compare previously published drag coefficients for grains classified using two different measures of grain shape: the Powers roundness factor, P, and the Corey shape factor, S_f. The Powers roundness factor describes the angularity of the grain boundary[51], with P = 6 for smooth, rounded grains and P = 2 for very angular grains. In contrast, the Corey shape factor (defined in the main text) describes overall grain shape, which determines how projected area varies with orientation; S_f is 1 for spheres and closer to zero for flatter grains. Extended Data Fig. 2a shows trends of drag coefficient vs. S_f for a compilation of grains grouped by P. Each gray line in Extended Data Fig. 2a (P = 6, 3.5, and 2) represents the effect of gross grain shape on the normalized settling drag coefficient $C_{D_{\text{settle}}}/C_o$, where C_o is the drag coefficient of the volume-equivalent sphere, while controlling for grain boundary angularity. For grains with a given P, the decrease in the drag coefficient as sphericity increases scales approximately with $1/S_f$ (red

dashed line). For the smoothest grains with P = 6, for example, the relationship is well approximated by $C_{D_{\mathrm{settle}}}/C_o = 1/S_f$.

We assume that the effect of gross grain shape on drag is equivalent to the effect of settling orientation, because gross grain shape controls the projected area of a grain in a given orientation. Therefore, to calculate an effective drag coefficient that reflects increases in drag due to grain angularity and roughness but corrects for the effect of settling orientation, we divide the measured settling drag coefficient by a factor of $1/S_f$. This yields an effective "orientation-free" drag coefficient $C_D = S_f C_{D_{\mathrm{settle}}}$. The result is that, for example, two smooth, well-rounded grains (P = 6) with equal mass and volume but different gross grain shapes (e.g., a sphere versus an oblate ellipse) have the same C_D (Extended Data Fig. 2b). For rougher or more angular grains (P < 6), C_D is greater than the drag coefficient of a volume-equivalent sphere.

Flume experiments

We chose five different materials for the flume experiments (Fig. 2) with similar densities and sizes but different shapes. Extended Data Table 1 lists their key properties. We carried out the experiments in the narrow flume facility in the River Dynamics Laboratory at Simon Fraser University. The experimental setup (Extended Data Fig. 3) consisted of a flume 4 m long, 45 cm tall, and 1 cm wide (slightly larger than two grain diameters) tilted 3 degrees from horizontal. Water was recirculated at a fixed discharge with a pump, creating a flow with a mean velocity of approximately 1 m/s. The mean water depth was 10 cm, and the mean hydraulic radius was 0.5 cm. This corresponds to a Reynolds number of 5000 and a Froude number close to 1. We fed grains into the flume at a fixed rate with a grain hopper, making the sediment flux a fixed input parameter in each experiment. The base of the flume was a fixed bed of grains of different sizes.

In each experiment, grains formed an aggrading bed until a steady-state bed slope was reached. The bed slope could be larger or smaller than that of the flume and ranged from 1.8º to 7.4º with a mean of 3.5º across all experiments. The minimum bed depth was 5 cm (10 grain diameters). Once at steady state, the experimental observations commenced. Observations consisted of measuring the mean bed and water slope in the middle 2.5 m of the flume and measuring the mass flux of grains into a sediment trap at the end of the flume. To measure mass flux, the sediment trap was allowed to fill for a set period of time ranging from 30 to 900 seconds, depending on the mass flux. We dried and weighed the collected grains and calculated the mass flux as the measured mass divided by the accumulation period. The final mass flux for each experiment is the mean of at least 3, and on average 10, individual mass measurements. We then divided the mass flux by the channel width and grain density to convert it to a volume flux per unit width.

We calculated bed shear stress using the depth-slope approximation for steady, uniform flow, $\tau = \rho g R S$, where *R* is hydraulic radius. By using the hydraulic radius, we remove the need for a wall correction. However, to verify that this provides a good estimate of the bed shear stress, we compare these shear stress estimates to shear stress estimated by fitting the Law of the Wall to velocity profiles measured using particle image velocimetry (Extended Data Fig. 7). The two different approaches yield shear stress estimates that are proportional to one another but differ by a factor of approximately 3.5. This demonstrates that $\tau = \rho g R S$ provides a good relative estimate, e.g. doubling the boundary shear stress is accurately captured as a doubling of the product $\rho g R S$.

Due to the narrow width of the flume, we would ideally use the bed slope rather than the water surface slope for *S*. However, the water surface slope could be measured more reliably than the bed slope due to persistent grain motion along the bed. Noting a consistent approximately 1% grade offset between the bed slope and the water surface slope, we estimated the bed slope in each experiment by subtracting 1% grade from the measured water surface slope.

Grain characterization

Grain density measurements. We measured grain density by massing a sample of 15-40 grains in an empty 10 mL vial and again after the vial had been filled with water to the 10 mL mark. The difference between the mass of the vial when empty and when filled with water was used to calculate the volume of the grain sample. The procedure was repeated 3 times for each grain type.

Grain shape measurements. We characterize grain shape with three mutually perpendicular lengths (a ≥ b ≥ c) (ref. 52) using the minimum bounding box method[53]. Extended Data Fig. 4 shows distributions of grain shape measurements for the materials with variable grain shape. The spheres can be characterized by a single diameter (mean and standard deviation 4.9 ± 0.05 mm), as there was no variation in shape between grains. The faceted ellipsoids, which also had no variation in shape between grains, are circular in a cross-section perpendicular to their shortest axis, giving dimensions of a = b = 6.0 ± 0.1 mm, c = 5.0 ± 0.1 mm. The rectangular prisms are somewhat regular, with a square cross-section perpendicular to the longest axis which has consistent dimensions from grain to grain. The variation in grain shape lies nearly entirely in the length of the longest axis (a = 4.4 ± 0.77 mm, b = 3.4 ± 0.27 mm, c = 3.4 ± 0.2 mm). The rounded chips consist of smooth, rounded glass pieces with random shapes, and tend to have one dimension that is substantially shorter than the other two (a = 8.7 ± 2.19 mm, b = 5.7 ± 1.02 mm, c = 3.5 ± 1.00 mm). The natural river gravel was sourced from a beach near Vancouver, Canada, and sieved to a narrow grain size distribution (4.0 ≤ b ≤ 5.6 mm). We scanned approximately 1600 grains with a microCT scanner, providing high-resolution shape data. We then measured the lengths a, b and c directly from the scanned shapes (a = 5.8 ± 1.07 mm, b = 4.4 ± 0.50 mm, a = 3.3 ± 0.42 mm). The faceted ellipsoids, rounded chips, and rectangular prisms have a hole through the middle of each grain, which we measured and accounted for in the grain density calculation by assuming the hole is water-filled during sediment transport.

Drag coefficient measurements*.* The drag coefficient of a settling grain, $C_{D_{\text{settle}}}$, is calculated from the average settling velocity, w_s, for each granular material using the relation[54]

$$C_{D_{\text{settle}}} = \frac{4}{3}\frac{Rgd_o}{w_s^2} \tag{14}$$

which assumes that drag force balances the submerged weight of a grain settling in still water at terminal velocity. The settling velocity of a grain was measured by releasing it just beneath the surface of a tank of still, room-temperature water and filming its descent with a high-speed camera. Velocity was measured once the grain had stopped accelerating. This was repeated for 20-50 grains for each grain type, allowing for the characterization of the mean and standard deviation of the settling velocity. Extended Data Fig. 5 shows distributions of measured settling velocities.

Calculated drag coefficient of volume-equivalent spheres*.* We calculated the drag coefficient for a volume-equivalent sphere, C_o, using the estimated volume-equivalent sphere settling velocity and equation (14). The volume-equivalent sphere settling velocity is estimated using the empirical equation[24]

$$\log W_* = -3.76715 + 1.92944\log D_* - 0.09815(\log D_*)^2 - 0.00575(\log D_*)^3 + 0.00056(\log D_*)^4 \tag{15}$$

where $W_* = w_o^3/(Rg\nu)$, $D_* = Rgd_o^3/\nu^2$, and ν is the kinematic viscosity of water.

Coefficient of static friction measurements. We estimated the coefficient of static friction from the angle of repose, ϕ, of the different granular materials using $\mu_s = \tan\phi$ (ref. 55). We measured the internal angle of repose of each grain type using the fixed funnel method[56]. For each grain type we poured grains slowly from a height of a few centimetres onto an elevated disk with a diameter of 12 cm (approximately 24 grain diameters) and a rim height of 1 cm (approximately 2 grain diameters). We continued to pour grains until a conical pile grew to the diameter of the elevated disk and small avalanches began to occur, indicating that a steady-state slope had been achieved. Using OpenCV[57] image processing software, we extracted the silhouette of the pile and fit a line to the silhouette on either side, excluding the parts of the pile close to the base or close to the peak (Extended Data Fig. 6). We repeated this procedure 3 to 6 times for each granular material. A few piles had distinctly convex or concave sides and were excluded from the analysis. The average slope of the fitted lines for each material was taken as the angle of repose (6 ≤ n ≤ 12) (Extended Data Table 1).

Data availability

The experimental flume data and measurements of grain properties used to support the conclusions and generate the figures in the paper will be deposited in a public repository (e.g., Figshare or Dataverse) before publication.

Code availability

The code used to process the data will be included alongside the data in the public repository.

Acknowledgments

The authors thank Catherine Johnson and Mark Jellinek for logistical support, Matthew Rushlow and Marjorie Cantine for assistance with grain shape measurements, and Michael Church for discussions of grain shape and flume experiments. Research was sponsored by the Army Research Laboratory and was accomplished under Grant Number W911NF-16-1-0440. The views and conclusions contained in this document are those of the authors and should not be interpreted as representing the official policies, either expressed or implied, of the Army Research Laboratory or the U.S. Government. The U.S. Government is authorized to reproduce and distribute reprints for Government purposes notwithstanding any copyright notation herein. S.J.B. was partly supported by a grant from the NASA FINESST program. The experimental facility was constructed using a Canadian Foundation for Innovation Leaders Opportunity Fund grant to J. V.

Author contributions

E.D., J.T.P., K.K. and J.G.V. conceived of the project. E.D. developed the grain shape theory with input from J.T.P. E.D., J.T.P., J.G.V., S.J.B. and R.B. performed laboratory flume experiments. E.D. measured grain density, shape, and drag coefficients. E.D. and J.T.P. measured grain friction coefficients. E.D. analyzed the experimental data with input from the other authors. E.D. and J.T.P. wrote the paper with input from the other authors.

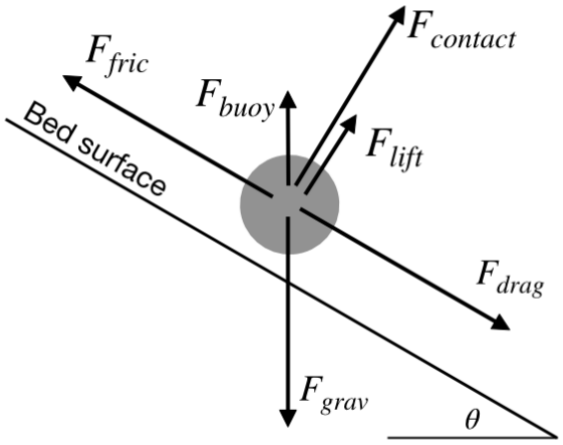

Extended Data Fig. 1 | Free body diagram of a single grain on a bed with inclination θ.

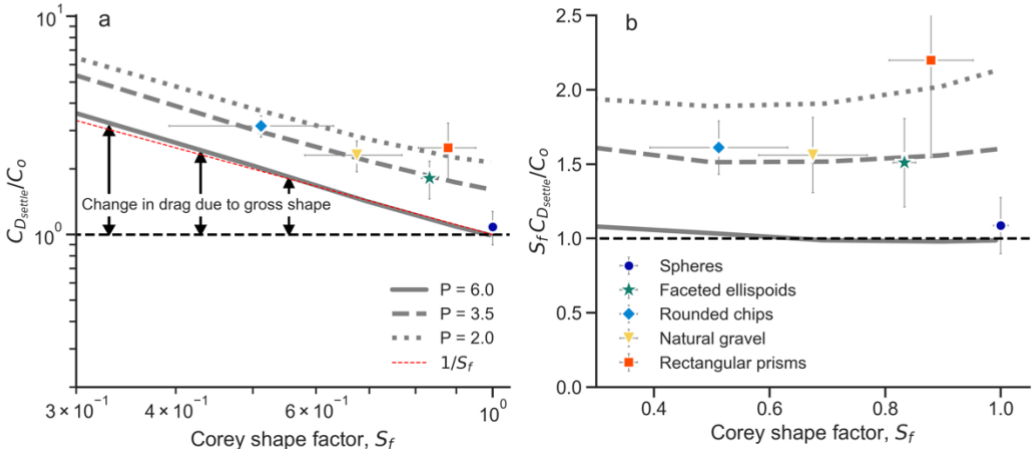

Extended Data Fig. 2 | Effects of different aspects of grain shape on fluid drag coefficient. a, The measured drag coefficient of a grain settling in still water, $C_{D_{\text{settle}}}$, relative to the calculated drag coefficient of the volume-equivalent-sphere, C_o, as a function of the Corey shape factor. Colored points show the materials used in our experiments. Gray lines are fits to a large compilation[24] of single-grain settling experiments for different Powers roundness factors[51] (P). Red dashed line is the trend $1/S_f$ for comparison. **b**, Normalized orientation-free drag coefficient as a function of Corey shape factor. Gray lines are fits to the same compilation as in **a**. The materials used in this study are also shown for reference. We note that the rectangular prisms are substantially more angular than the other materials.

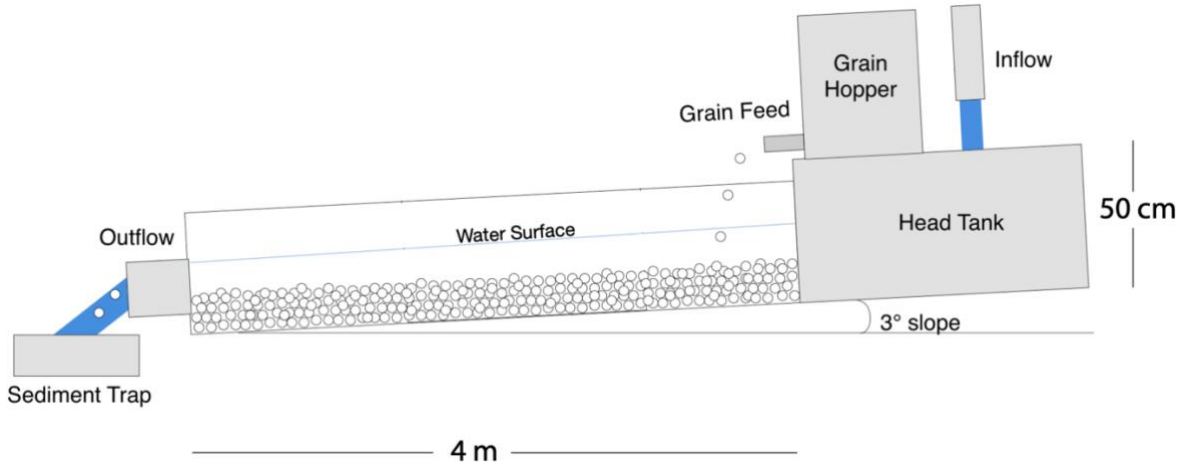

Extended Data Fig. 3 | Schematic of laboratory flume. Measurements of bed and water surface slope were made in the middle 2.5 m of the flume, where there were no visible entry or exit effects on grain motion. The flume is inclined 3°, but the sediment bed can develop a slope that is either steeper or less steep than the flume.

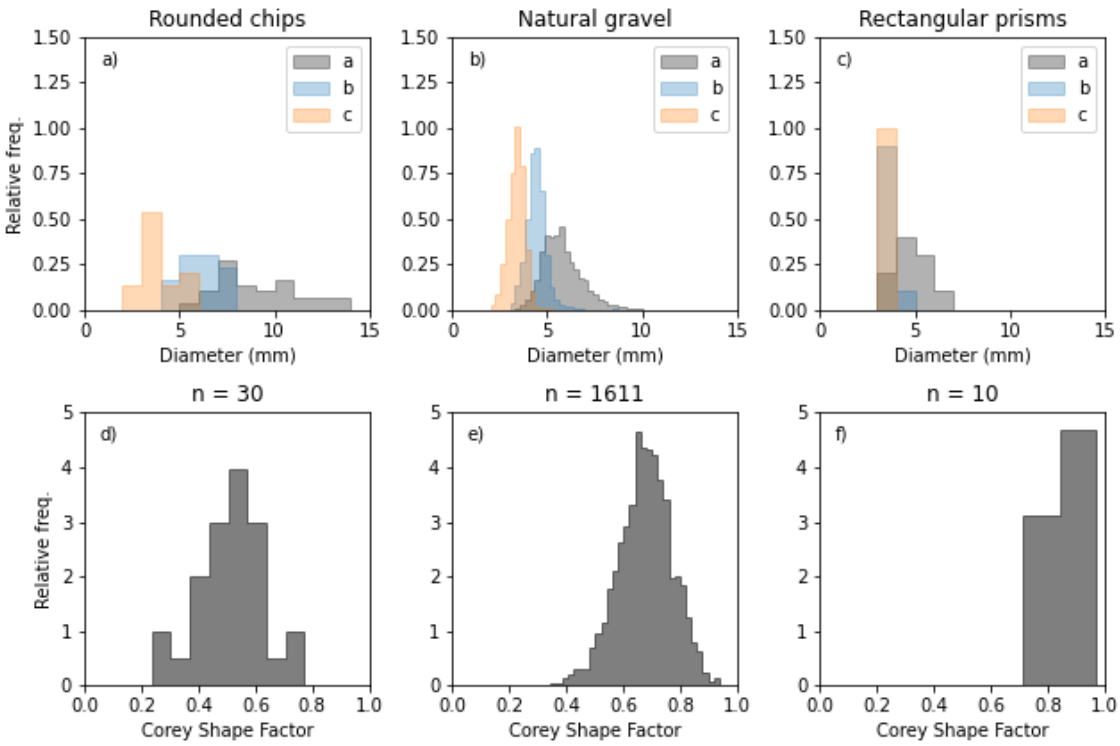

Extended Data Fig. 4 | Shape distributions of granular materials with variable grain shapes. **a-c**, Histograms of the three axes (a, b, and c) used to characterize grain shape. **d-f,** Corresponding histograms of the Corey shape factor. n is the sample size for each grain type.

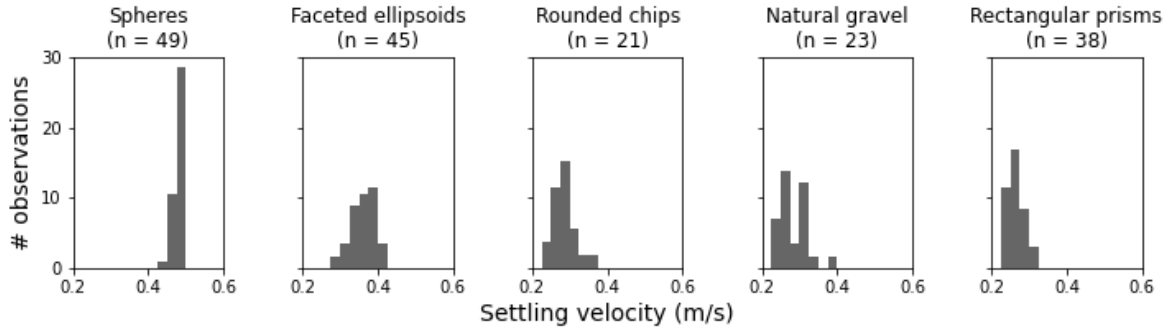

Extended Data Fig. 5 | Distributions of settling velocities for the grain types used in flume experiments. n is the sample size for each grain type.

526

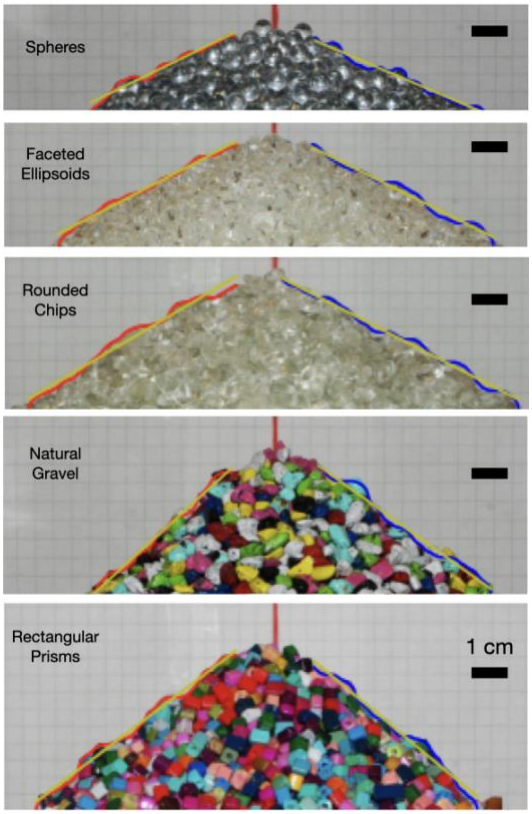

Extended Data Fig. 6 | Measurement of the angle of repose of experimental materials. Blue and red lines are the right and left edges of the pile silhouette extracted with image analysis. Yellow lines are least-squares fits to these edges used to estimate the angle of repose. Vertical red line at the centre of each image is a plumb line used to determine the direction of gravity.

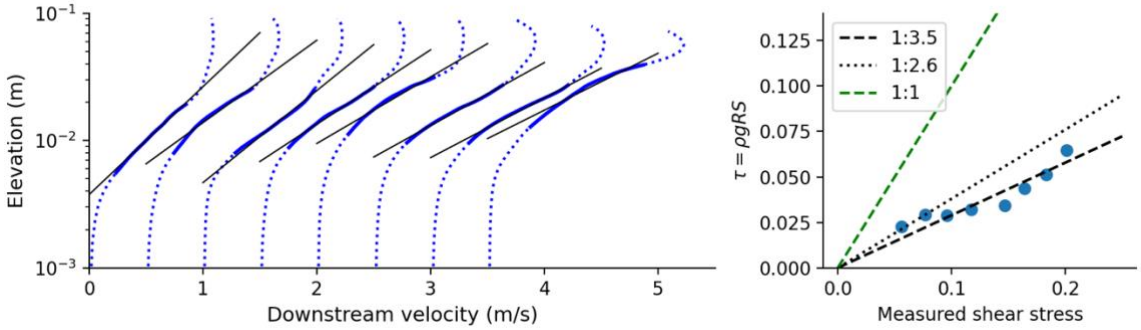

Extended Data Fig. 7 | Comparison of boundary shear stress estimates from two different methods. For a subset of the experiments with spheres, flow velocity was measured using laser particle image velocimetry. Profiles of fluid velocity in the flow direction as a function of distance above the grain bed (blue dotted lines), offset on the x-axis for visual clarity, are fit with the Law of the Wall (black lines), $u = (u_*/\kappa)\ln(30z/d)$ where κ is the von Karman constant (0.4), d is the grain diameter, and $u_* = \sqrt{\tau/\rho}$ is the shear velocity that we compare to the estimated shear stress, $\tau = \rho g R S$. The profiles are fit over the range of 20% of the maximum velocity to 80% of the maximum velocity (solid blue lines).

Extended Data Table 1 | Grain properties. Measured grain density, measured grain dimensions a, b, and c, estimated volume equivalent sphere diameter d_o, measured mean settling velocity w_s, calculated settling velocity of the volume equivalent sphere w_o, the mean coefficient of drag $C_{D_{\text{settle}}}$ calculated from the settling velocity, the estimated orientation-independent drag coefficient $C_D = S_f C_{D_{\text{settle}}}$, the calculated drag coefficient of the volume equivalent sphere C_o, the particle Reynolds number $Re_p = w_s d/\nu$ associated with the settling experiments (where *d* is the mean grain diameter and ν is the kinematic viscosity of water), the mean measured angle of repose of the granular material ϕ, and the associated coefficient of static friction μ_s. All uncertainties are one standard error of the mean.

	Spheres	**Faceted ellipsoids**	**Rounded chips**	**Natural gravel**	**Rectangular prisms**
$\boldsymbol{\rho_s}$ (kg/m^3)	2558 ± 128	2412 ± 148	2349 ± 59	2471 ± 122	2392 ± 290
a (mm)	4.9 ± 0.05	6.0 ± 0.10	8.7 ± 2.19	5.8 ± 1.07	4.4 ± 0.77
b (mm)	4.9 ± 0.05	6.0 ± 0.10	5.7 ± 1.02	4.4 ± 0.50	3.4 ± 0.27
c (mm)	4.9 ± 0.05	5.0 ± 0.10	3.5 ± 1.00	3.3 ± 0.42	3.4 ± 0.20
$\boldsymbol{d_o}$ (mm)	4.9 ± 0.05	5.0 ± 0.11	5.7 ± 0.48	4.1 ± 0.41	3.9 ± 0.18
$\boldsymbol{w_s}$ (m/s)	0.486 ± 0.015	0.360 ± 0.027	0.286 ±0.025	0.285 ± 0.023	0.263 ± 0.018
$\boldsymbol{w_\circ}$ (m/s)	0.506 ± 0.043	0.484 ± 0.053	0.508 ± 0.023	0.433 ± 0.040	0.416 ± 0.094
$\boldsymbol{C_{D_{settle}}}$	0.43	0.73	1.24	0.99	1.05
$\boldsymbol{C_D}$	0.43	0.61	0.64	0.67	0.93
$\boldsymbol{C_o}$	0.400	0.334	0.202	0.280	0.370
$\boldsymbol{Re_p}$	4900	6000	8733	5775	4400
$\boldsymbol{\phi}$ (º)	24.7 ± 0.98	31.0 ± 3.08	33.2 ± 2.84	38.0 ± 2.19	40.7 ± 0.88
$\boldsymbol{\mu_s}$	0.46 ± 0.02	0.60 ± 0.05	0.65 ± 0.05	0.78 ± 0.04	0.86 ± 0.02
$\boldsymbol{S_f}$	1.0 ± 0.012	0.83 ± 0.02	0.51 ± 0.12	0.67 ± 0.09	0.88 ± 0.07
$\boldsymbol{C^*}$	1.09 ± 0.20	1.51 ± 0.40	1.61 ± 0.49	1.61 ± 0.45	2.20 ± 1.05
$\boldsymbol{\mu^*}$	1.04 ± 0.05	1.41 ± 0.19	1.55 ± 0.18	1.87 ± 0.16	2.08 ± 0.07

Methods References

51. Powers, M. C. A new roundness scale for sedimentary particles. *Journal of Sedimentary Petrology* 23, 117–119 (1953).
52. Krumbein, W. C. Measurement and geological significance of shape and roundness of sedimentary particles. *J Sediment Res* 11, 64–72 (1941).
53. Blott, S. J. & Pye, K. Particle shape: a review and new methods of characterization and classification. *Sedimentology* 55, 31–63 (2008).
54. Riazi, A. & Türker, U. The drag coefficient and settling velocity of natural sediment particles. *Comput Part Mech* 6, 427–437 (2019).
55. Metcalf, J. R. Angle of repose and internal friction. *Int J Rock Mech Min* 3, 155–161 (1966).
56. Al-Hashemi, H. M. B. & Al-Amoudi, O. S. B. A review on the angle of repose of granular materials. *Powder Technol* 330, 397–417 (2018).
57. Bradski, G. & Kaehler, A. *Learning OpenCV*. (2008).